

# Image-Aligned Dynamic Liver Reconstruction Using Intra-Operative Field of Views for Minimal Invasive Surgery

Muhammad Nadeem Cheema , Anam Nazir, Bin Sheng , Ping Li , Jing Qin , Jinman Kim , and David Dagan Feng , *Fellow, IEEE*

**Abstract**—During hepatic minimal invasive surgery (MIS), 3-D reconstruction of a liver surface by interpreting the geometry of its soft tissues is achieving attractions. One of the major issues to be addressed in MIS is liver deformation. Moreover, it severely inhibits free sight and dexterity of tissue manipulation, which causes its intra-operative morphology and soft tissue motion altered as compared to its pre-operative shape. While many applications focus on 3-D reconstruction of rigid or semi-rigid scenes, the techniques applied in hepatic MIS must be able to cope with a dynamic and deformable environment. We propose an efficient technique for liver surface reconstruction based on the structure from motion to handle liver deformation. The reconstructed liver will assist surgeons to visualize liver surface more efficiently with better depth perception. We use the intra-operative field of views to generate 3-D template mesh from a dense keypoint cloud. We estimate liver deformation by finding best correspondence between 3-D templates and reconstruct a liver image to calculate translation and rotational motions. Our technique then finely tunes deformed surface by adding smoothness using shading cues. Up till now, this technique is not used for solving the human liver deformation problem. Our approach is tested and validated with synthetic as well as real *in vivo* data, which reveal that the reconstruction accuracy can be enhanced using our approach even in challenging laparoscopic environments.

**Index Terms**—3D reconstruction, liver deformation, minimal invasive surgery, keypoint mesh, field of view.

Manuscript received October 26, 2018; accepted November 28, 2018. Date of publication November 30, 2018; date of current version July 17, 2019. This work was supported in part by the National Natural Science Foundation of China under Grant 61872241 and Grant 61572316, in part by the National Key Research and Development Program of China under Grant 2017YFE0104000 and Grant 2016YFC1300302, in part by the Macau Science and Technology Development Fund under Grant 0027/2018/A1, and in part by the Science and Technology Commission of Shanghai Municipality under Grant 18410750700, Grant 17411952600, and Grant 16DZ0501100. (*Corresponding author: Bin Sheng.*)

M. N. Cheema and A. Nazir are with the Department of Computer Science and Engineering, Shanghai Jiao Tong University.

B. Sheng is with the Department of Computer Science and Engineering, Shanghai Jiao Tong University, Shanghai 200240, China (e-mail: shengbin@sjtu.edu.cn).

P. Li is with the Faculty of Information Technology, Macau University of Science and Technology.

J. Qin is with the Centre for Smart Health, School of Nursing, The Hong Kong Polytechnic University.

J. Kim and D. D. Feng are with the Biomedical and Multimedia Information Technology Research Group, School of Information Technologies, The University of Sydney.

Digital Object Identifier 10.1109/TBME.2018.2884319

## I. INTRODUCTION

TECHNOLOGY developments recently enable vast use of computer-assisted surgeries (CAS) in clinical procedures. While open surgery comprises of methods to directly access the affected organs, minimal invasive surgery (MIS) is carried out via a small incision to minimize surgical trauma and post-operative discomfort. It has led to faster recovery and cost-effective solution due to reduced hospitalization period [1]. The term hepatic laparoscopy refers to MIS performed in the liver using an endoscopic camera (laparoscope), which generates the field of views (FOVs) of a liver see (Fig. 1). Compared to open surgery [2], hepatic MIS offers a limited view of liver because the FOV of a laparoscope is typically very narrow. This constraint imposes a limitation on surgeon's navigation capabilities. As it is difficult to intelligently control the computer-assisted operations for observing beyond exposed intra-operative liver motion and morphology [1], [3]–[5]. During MIS, the abdominal cavity is filled with carbon dioxide gas (pneumoperitoneum) to create a working volume. Because of pneumoperitoneum and surgical manipulation such as the touch and pressure of laparoscopic camera, the liver shifts and deforms [6]. The surgical navigation grounded on pre-operative images enforces a surgeon to operate on verbal estimation and experience. The limitation of MIS to deliver similar visualization of pre-operative and intra-operative environments not only tempts greater mental workload on surgeons but also leads to inappropriate post-operative results [7].

Over more than two decades of practice, neurosurgery was the first field in which CAS become a standard procedure. Nowadays, nearly all computed assisted surgeries for brain integrate such a feature. The integration of MIS in various surgical fields has also reported such as dental surgery [8], orthopedics and ear nose throat (ENT). However, for all the mentioned fields, the structure of an organ is either rigid or semi-rigid. On the contrary, in the soft body parts surgery, organs undergone to deformation due to breathing and anatomical changes. It involves the physiological organ motion or of tissue change due to growth or disease patterns; as a result, CAS has little used and only a few laparoscopic interventions have been experimented on humans. The earliest attempt on the abdomen shows the ultrasound images through the head-mounted display [9]. In laparoscopy, surface-based methods [10] are widely used instead of other available

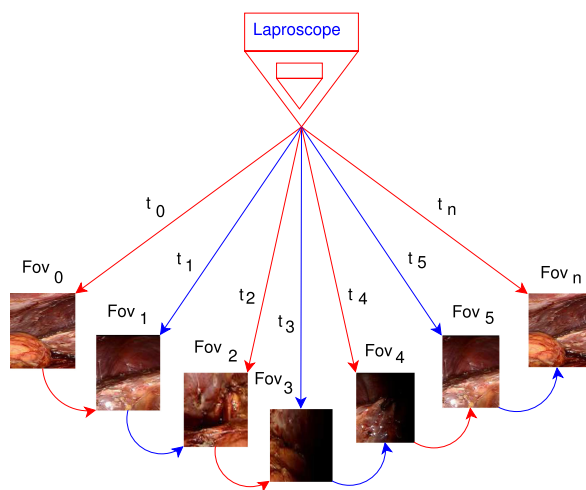


Fig. 1. Overlapping intra-operative FOVs taken at  $t_0$  to  $t_n$ , with respect to variable laparoscope camera positions (FOV<sub>0</sub>: superior view, FOV<sub>1</sub>: inferior view, FOV<sub>2</sub>: anterior view, FOV<sub>3</sub>: posterior view, FOV<sub>4</sub>: right view, FOV<sub>5</sub>: left view).

methods such as interactive approaches [11], [12], point-based registrations [13], and volume-based methods [14]. The interactive methods offer negative results for surgical workflow due to their dependence on manual methods, while point-based registration is now obsolete and seems to receive a lesser attention from researchers. Whereas, the volume-based techniques require additional hardware which is impractical [15]. The brief introduction of shape to shape and shape to volume is presented by [16]. A study on kidney surface reconstruction accuracy was published by [17]. Similarly, many researchers have reported the parallel work on rigid organs [18]. An attempt to carry out non-rigid registration on realistic phantom of the liver is presented by [19].

In the surface-based reconstruction paradigm, manual procedures are reported by [20]. Moreover, semi-automatic methods are presented in the literature by [21]. Such approaches are time consuming and still do not fill the challenges of laparoscopy. In case of CAS, one of the limitations is that the organs are very less exposed, therefore both the inner and critical parts of the organs remain invisible during surgery and make reconstruction process less reliable. Many approaches are presented to handle this issue such as [22] presented a spring mass system based on B-spline and thin plate splines. Recent work of [23] achieve up to 1mm of root mean square (RMS) error on silica and liver phantom. Other solutions regarding the issue are contour detection, use of biomechanical model for the entire organ, sparse reconstruction based on learned structured dictionary [24], [25]. The elementary limitation of the state-of-the-art for surface-based approaches is incompleteness of the reconstructed surface [26]. As laparoscopy can provide only the local view of the organ, the existing techniques are less reliable, experimented on phantoms thus impractical [27]. So, for medical experts, the hectic procedure of estimation remains challenging. Moreover, validation of CAS techniques is also one of the main concerns. Indeed, significant efforts have been made to solve this issue, yet phantoms and models [28], [29] are not compared to real organs.

To address the above-mentioned shortcomings, several research techniques have been developed for laparoscopy. Shape from motion (SFM) has shown efficacy in recovering 3D surfaces of the abdomen [30] and heart [31]. Several frameworks use SFM technique for achieving 3D reconstruction [32] based on Simultaneous Localization and Mapping (SLAM) [33], [34]. However, SLAM methods are well suited for rigid surfaces. The state-of-the-art methods implementing SLAM technique are based on an assumption that the physical world is static. However, in anatomical environment such as soft body part deformation, dense surface reconstruction introduces an increased complexity of non-rigid modeling. SLAM algorithm [35] requires a long period of time to establish a set of 3D landmarks using a repeated matching strategy for an image. Therefore, robustness and reconstruction accuracy are directly proportional to accurate matching. Hence non-rigid tissue surfaces without texture or detectable features will require additional approaches such as SFS algorithms for complete information [1]. Deformable shape from motion (DSFM) also, has been attempted previously in rendering 3D surfaces during laparoscopy [36]. The limitation of DSFM is its incapability to densely cover the liver surface with feature correspondences because human liver tends to be shown repeated structures during MIS due to its texture-less surface [35]. Thus, automatic feature detection and matching techniques of DSFM has proven to be less precise for recovering 3D surface details. Shape from shading (SFS) is well-known technique practiced in laparoscopy, because the laparoscopic camera has a constant relative pose under a light source.

However, SFS is mainly based on an assumption that laparoscopic camera projection models are known. So, it is hard to attain significant 3D reconstructions due to the complex and varied reflection on the liver tissues. Recently, deformable shape from motion and shading (DSFMS), a combination of SFS and DSFM has been proven to be useful to recover rigid and deformed surfaces [37], [38]. However, correspondence establishment is still an open issue in such methods. Furthermore, during laparoscopy, liver tissue may have homogeneous texture (texture-less). Due to which, laparoscopic images tend to show repeated structures, and thus beat current matching methods and make DSFMs automatic salient feature detection and matching difficult. According to our scope of knowledge, no such technique is available which is based on a fully automatic method to handle 3D surface reconstruction issues [26]. In this paper, we have implemented the deformable structure from motion. This technique has been reported in the literature from past ten years and has numerous application usages; one of them is laparoscopy [30].

To overcome aforementioned limitations, this article introduces an effective technique for liver surface reconstruction. The proposed technique uses intra-operative deformed FOVs as an input, during laparoscopy, and reconstructs a 3D liver image from these FOVs. The resultant deformed reconstructed liver image is comparable to its pre-operative model. To enhance the visual capabilities of medical experts, the reconstructed images can be shown to surgeons during laparoscopy on a computer screen to achieve better depth perception. To the best of our

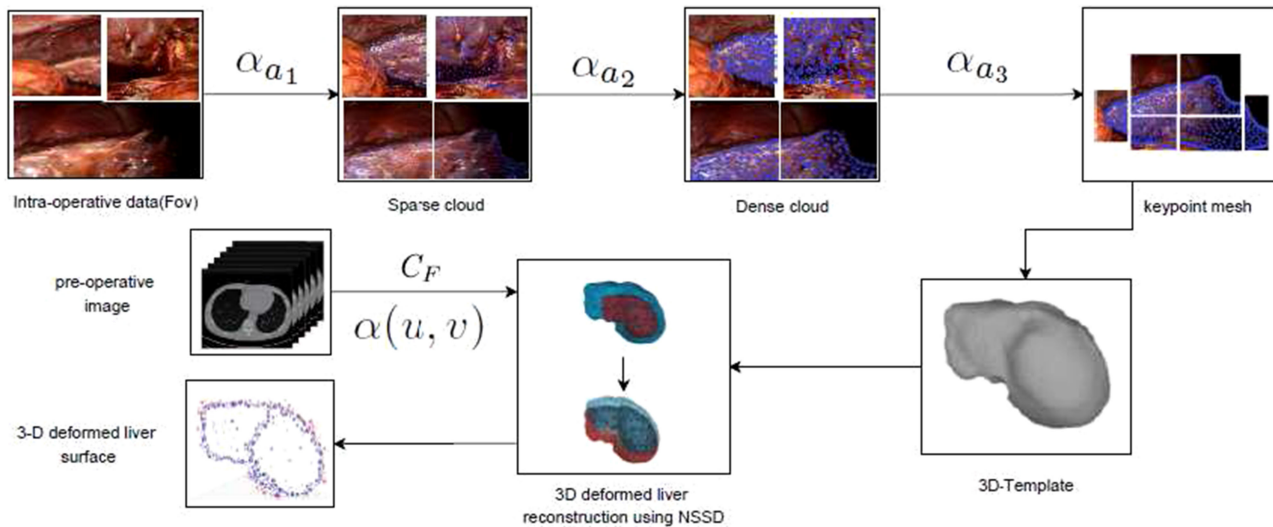


Fig. 2. Modeling a 3D template. From left to right: With intra-operative FOVs having functions of sparse cloud  $\alpha_{a_1}$ , dense cloud  $\alpha_{a_2}$ , and keypoint mesh  $\alpha_{a_3}$  to reconstruct 3D template using mapping function, matching points and detected corners. Correspondence function  $C_F$  with  $\alpha(u, v)$  albedo of the liver surface maps deformation between the template and the pre-operative image using transformation  $F$  to reconstruct the deformed liver surface.

knowledge, the proposed method is a comprehensive, mathematical and statistical study to be enacted in the laparoscopic procedure for human liver. It enables a real-time display of the liver deformation. Unlike numerous methods implemented to simulate soft tissue deformations so far, the designed technique considers the organ specificity. Our work makes the following four main contributions:

- Modeling a 3D template of keypoints from multiple overlapping intra-operative FOVs to solve laparoscopic camera pose and image geometry (see Fig. 2).
- Liver surface reconstruction by employing motion cues of SFM via 3D template and pre-operative data (see Fig. 3).
- Estimate liver deformation by finding best correspondence between 3D template and reconstructed liver image to calculate translation and rotational motions along with shading cues.
- Incorporate estimated deformation in resultant reconstructed liver image for its better visualization and comparison to pre-operative data.

## II. METHODS

SFM is a passive monocular technique and does not require hardware amendment to standard laparoscopes [6]. It uses the superficial image motion as a cue to recover depth. In SFM, the camera movement is unknown, and the detected surface could possibly deform between the input images [39]. In our approach, the deformation in 3D liver reconstruction is determined from a series of overlapping FOVs taken from different angles with a moving laparoscope as shown in Fig. 4. In this research, we have used template-based SFM, instead of classical rigid SFM to solve liver surface deformations [6], [40], [41]. Our approach first model a 3D template of keypoints, reconstruct the liver surface using a 3D template, estimate and incorporate the deformation in a reconstructed image so that it is comparable to

pre-operative image. Further explanation for each step of the methodology is given below and also depicted in Fig. 5.

### A. Dataset Details

To demonstrate the practicability of learning compact visualization from large-scale 3D volumetric data, the proposed method has been evaluated on two unpublished datasets. First, pre-operative dataset consists of 75 CTA volumes and their correspondingly labeled ground truth collected from the co-operative hospital located in Shanghai, China. The ratio is 2:1 (50 to test: 25 to validate). We divided volume in to  $128 \times 128 \times 128$  size small sub-volumes, resulting in millions of sub-volumes (images) for our testing purpose and same division for the validation purpose. The manual labeling of the dataset for validation purposes is done by an expert medical physician, for 25 CTA it cost around fifteen days to complete manual labeling, five to six hours for each CTA. The number of a voxel in our pre-operative dataset were around  $300 \times 350 \times 300$ , and the spacing between voxel is between (0.75 mm, 0.75 mm, 0.75 mm) to (1 mm, 1.5 mm, 1.5 mm). In preprocessing step, the volumes have been re-sampled to the spacing of (1.5 mm, 1.5 mm, 1.5 mm), and then be split into slices of size  $128 \times 128 \times 128$ . Second is intra-operative dataset comprises of 5162 intra-operative images taken during laparoscopy. We have classified our intra-operative dataset into five classes named as anterior\_view, posterior\_view, superior\_view, inferior\_view and side\_view. All images from above-mentioned classes are used for testing. For validation, we have randomly selected 25 images from each class.

### B. Modeling a 3D Template From Intra-Operative FOVs

We have determined the laparoscopic camera position and 3D template geometry through automatic identification of

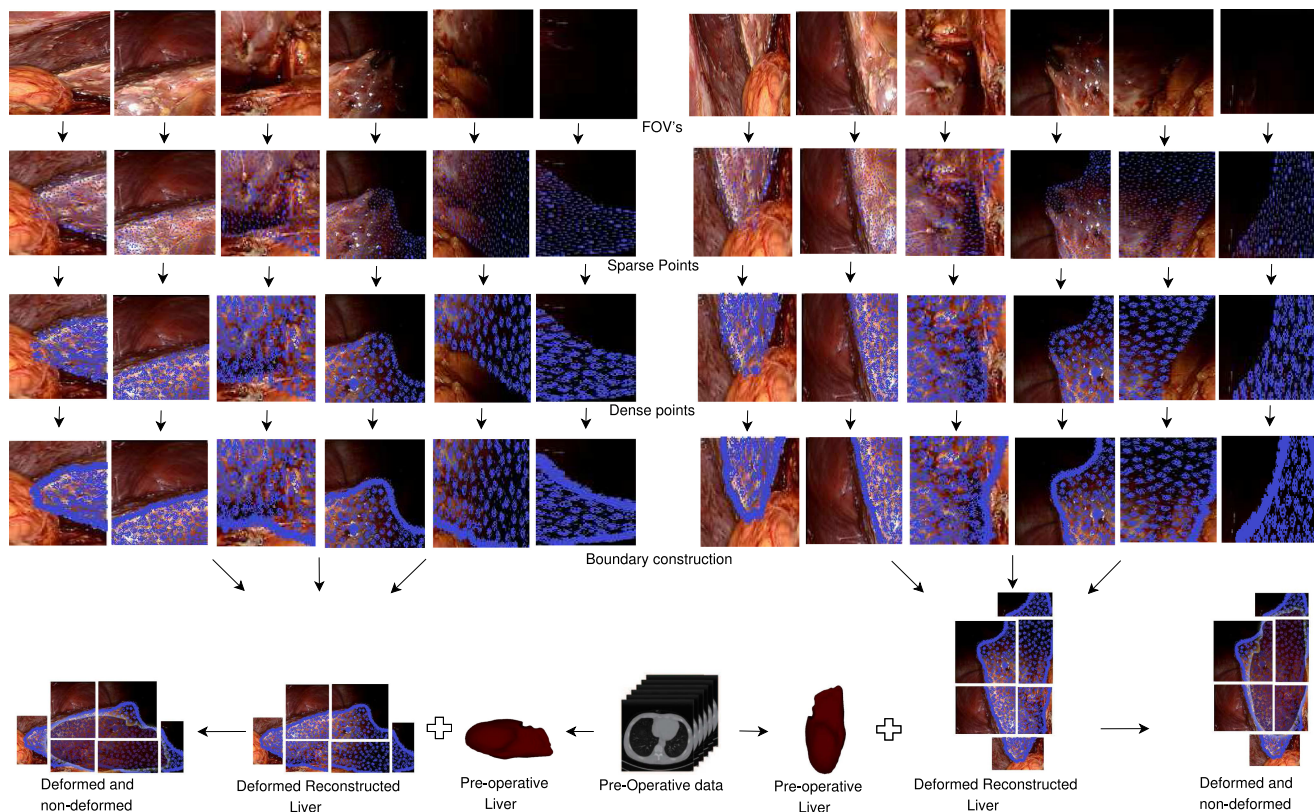


Fig. 3. Qualitative results of our proposed approach on liver surface reconstruction with deformation. From top to bottom: intra-operative FOVs with sparse points, dense points detected in first and second layer. Third layer is showing boundary formation using detected keypoints mesh. Last layer is showing comparison between pre-operative CTA volumes and reconstructed liver to incorporate deformation in the results.

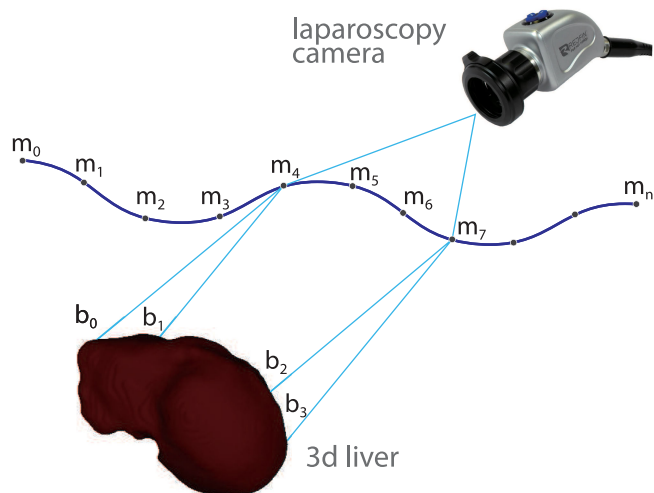


Fig. 4. Small errors on image plane  $m_0$  to  $m_n$  leads to large errors in resultant 3D space  $b_0$  to  $b_3$ .

identical features in multiple FOVs as shown in Fig. 2. These features are traced from multiple FOVs, permitting preliminary approximations of the laparoscopic camera positions and 3D template coordinates. We have used a prevalent solution, Scale Invariant Feature Transform (SIFT) for feature extraction [42]

(see Fig. 6). We have implemented in SFMToolkit3 using the SiftGPU algorithm [43]. The SIFT; first detects the keypoints over all scales and locations in each FOV, then represents the local FOV's local gradient into an illumination free form. Afterward, it generates distinctive feature descriptors for matching keypoints with the respective datasets of FOVs [43]. In our setup, for any FOV, a corner is a keypoint for which there are two dominant and different edge directions in a local neighborhood. For the proposed approach, the detected number of keypoints depend on the quality and resolution of a FOV. Hence, the spatial resolution of the FOV is directly proportional to the density of resultant mesh of keypoints. Table I summarizes the output of our keypoints feature extraction for experimental setup of SIFT extractor. Following keypoint detection, next step is the mesh generation of keypoints for modeling 3D template described in Fig. 2.

For 3D template generation from a mesh of keypoints, we have jointly used the ideas of bundle adjustment and triangulation. The bundler refines visual reconstruction and generates a sparse keypoint cloud for optimal 3D structure whereas triangulation estimate laparoscopic camera pose [44] shown in Fig. 5. The bundle adjustment minimizes the total reprojection error with respect to all 3D points and laparoscope parameters. Let us consider some 3D points are shown in  $f$  FOVs, and let  $a_{ij}$  be the project of  $i$ th point on FOV  $j$ . Let  $b_{ij}$  denotes the binary variable which is 1 if point  $i$  is visible in FOV  $j$  and 0 otherwise.

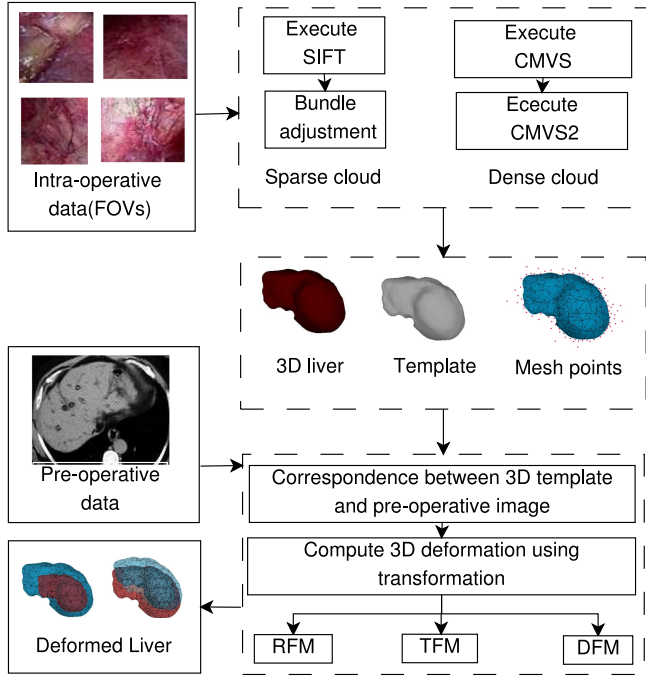


Fig. 5. The work flow of our approach. From top to bottom: Keypoint extractions with SIFT, 3D mesh points and bundle adjustment are shown. Finally, estimation of liver deformation by finding best correspondence between 3D template and reconstructed liver image to calculate translation and rotational motions along with shading cues (TFM, RFM, and DFM).

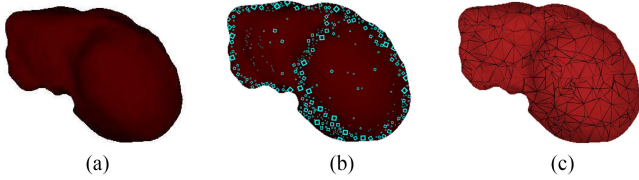


Fig. 6. (a) 3D liver model extracted from pre-operative CT scans using Slicer. (b) Scale Invariant Feature Transform (SIFT) decomposes a liver image into a database of "keypoint descriptors". Lines represent individual keypoints, proportionally scaled according to the radius of the image region (pixels) containing the keypoint and blocks represent the detected corner. (c) 3D liver model representation of triangulated approximation for estimating laparoscopic camera pose to detect the geometry of 3D template.

Here, we assume each laparoscope position is parametrized by a vector  $c_j$ , and 3D point  $i$  by a vector  $d_i$  than reprojection error can be define formally as:

$$\min_{c_i, d_j} \sum_{i=1}^e \sum_{j=1}^f b_{ij} d(p(c_i, d_j) a_{ij})^2 \quad (1)$$

Here, the projection of point  $i$  on FOV  $j$  is represented by  $p(c_i, d_j)$ . We have used nearest neighbor search (NNS) algorithm for sparse cloud generation. For our setup, NNS match keypoints in multiple FOVs taken from different angle and nominated keypoints are explicitly labeled as tracks [45] as shown in Fig. 2. At least three FOVs should contain a minimum of two keypoints for the sparse point cloud. This criterion

automatically removes the blur areas in FOVs. Along with bundler output, we have used the triangulation technique for estimating the laparoscopic camera calibration.

To formally define the triangulation for our approach let us assume  $\alpha$  is used to calculate a 3D space point  $Y$  from a point correspondence  $V$  to  $V'$  and two camera matrices  $R$  and  $R'$ , for which we can compute a 3D point  $Y$  as:

$$Y = \alpha(V, V', R, R') \quad (2)$$

For Eq. (2), a transformation  $T$  is said to be invariant if:

$$\alpha(V, V', R, R') = T^{-1} \alpha(V, V', RT^{-1}, R'T^{-1}) \quad (3)$$

Assuming a gaussian noise, the real values of corresponding FOV points should be  $V^*$  to  $V^{*o}$  are similar to measured points  $V$  to  $V'$  and fulfill the requirement of  $V^{*oT} F v^*$ . Here, to calculate the function that minimize the values of points  $V^*$  and  $V^{*o}$  we can say that:

$$d(V, V^*)^2 + d(V^o, V^{*o}) \quad (4)$$

Where,  $d(V, V^*)$  is used to represent Euclidean distance and with epipolar constraint it can be written as:

$$V^{*oT} F v^* = 0 \quad (5)$$

From above metrics, the points  $V^*$ ,  $V^{*o}$  are the most probable values for accurate point correspondences between two FOVs. From above formulation, we have deduced  $Y$  as positions of required 3D points in space as an estimation of our laparoscopic camera positions as shown in Fig. 2. Similarly, for all other FOVs, a new set of 3D points are triangulated with a different camera resection to estimate the camera calibration.

Next, the estimated camera positions are used as input to generate a dense keypoint cloud using Clustering View for Multi-view Stereo (CMVS) and Patch-based Multi-View Stereo (PMVS2) algorithms [46] see in Fig. 5. The CMVS breakdown the overlapped FOVs into clusters of controllable size, while PMVS2 increase the point density of individual clusters and generate a dense cloud. The resultant keypoints are connected to form a mesh in the form of 3D liver template with  $M_h$  faces  $h$  and  $K_u$  vertices  $u$  given by the set of triangulated 3D points as shown in Table I.

### C. Liver Surface Reconstruction Using 3D Template and Pre-Operative Data

We have used correlation method, for solving the correspondence problem. The employed correlation finds correspondence points by comparing thresholded signed gradient magnitudes at each pixel of 3D liver template and 3D liver model extracted from pre-operative data. This method depends on two geometric constraints to compute the gradient magnitude. The first one is an epipolar constraint, which converts the 3D search spaces to one-dimensional. The second constraint is based on an assumption that for each FOV, the gradient magnitude remains constant in small image patches. We have matched the small image regions on two FOVs along the epipolar line based on the two aforementioned constraints. For our setup, the 3D template and pre-operative image are rectified, so the search line

TABLE I

EXPERIMENTAL SETUP AND SFM OUTPUT FOR SIFT, BUNDLE ADJUSTMENT WITH RESPECT TO MULTI-VIEW OF INTRA-OPERATIVE FOVS. LAP STANDS FOR LAPAROSCOPIC IMAGE MODALITY FOR ANY FOV

No.	Position	Experiment	Modality	No of FOVs	Edges detected	Corners detected	Sparse points	Dense points	Total keypoints
1	Anterior_view	exper_1	LAP	560	$6.1*(10)^4$	$8.3*(10)^5$	$5.9*(10)^3$	$9.2*(10)^8$	$14.4*(10)^9$
		exper_2	LAP	529	$5.4*(10)^4$	$3.2*(10)^5$	$5.2*(10)^3$	$11.2*(10)^8$	$8.6*(10)^9$
2	Posterior_view	exper_1	LAP	523	$9.1*(10)^4$	$7.3*(10)^5$	$6.3*(10)^3$	$8.2*(10)^8$	$16.4*(10)^9$
		exper_2	LAP	638	$2.9*(10)^4$	$7.2*(10)^5$	$3.6*(10)^3$	$6.2*(10)^8$	$9.11*(10)^9$
3	Superior_view	exper_1	LAP	340	$5.8*(10)^4$	$2.9*(10)^5$	$3.9*(10)^3$	$7.3*(10)^8$	$8.7*(10)^9$
		exper_2	LAP	510	$4.2*(10)^4$	$4.3*(10)^5$	$2.9*(10)^3$	$7.1*(10)^8$	$8.5*(10)^9$
4	Inferior_view	exper_1	LAP	360	$3.8*(10)^4$	$4.3*(10)^5$	$4.6*(10)^3$	$11.2*(10)^8$	$7.11*(10)^9$
		exper_2	LAP	830	$3.4*(10)^4$	$9.2*(10)^5$	$4.5*(10)^3$	$9.2*(10)^8$	$12.6*(10)^9$
5	Side_view	exper_1	LAP	350	$8.2*(10)^4$	$2.7*(10)^5$	$8.2*(10)^3$	$9.3*(10)^8$	$10.9*(10)^9$
		exper_2	LAP	520	$6.1*(10)^4$	$4.9*(10)^5$	$4.2*(10)^3$	$8.1*(10)^8$	$10.1*(10)^9$

in a 3D template is aligned vertically. As a result, search line is on the same location in 3D template as corresponding points are located in the pre-operative image. Thus, the horizontal distance between the corresponding points in our setup is termed as gradient magnitude.

In case of liver, we have various types of deformation involved, such as, due to  $CO_2$  gas insertion, surgical instrument manipulation, and respiratory motion. To incorporate all the deformations, we have applied extensible 3D motion along with correlation-based mapping. After finding correspondence, we have computed the rigid transformation of the initial 3D template to the pre-operative image. It is estimated as the average rigid transform which maps the pre-operative image correspondences to the 3D template mesh. We have incorporated transformation for our methodology using translation and rotational motion of the 3D points [47] shown in Fig. 5. The translation motion  $W$  in a deformed image is represented by  $3 \times 3$  matrix defined in Eq. (6). If  $x$  is a 3D point which represented by  $x = (x_1, x_2, 1)$ , we can write  $W$  as:

$$W = \begin{pmatrix} 1 & 0 & -x_1 \\ 0 & 1 & -x_2 \\ 0 & 0 & 1 \end{pmatrix} \quad (6)$$

Angle  $\theta$  is rotation around an origin to position the epipolar  $i$  on  $x$ -axis. At origin the rotational motion is represented by matrix  $O$  of dimensions  $3 \times 3$  defined as [47]:

$$O = \begin{pmatrix} \cos \theta & -\sin \theta & 0 \\ \sin \theta & \cos \theta & 0 \\ 0 & 0 & 1 \end{pmatrix} \quad (7)$$

For some  $f$ , a  $L$  translated epipole  $i = (i_1, i_2, i_3)^T$  is rotated on the  $x$ -axis, if

$$OL_i \approx (1, 0f)^T \quad (8)$$

Computing the left-hand side of Eq. (8), we can obtain:

$$\sin \theta (i_1 - i_3 x_1) + \cos \theta (i_2 - i_3 x_2) = 0 \quad (9)$$

Above equation allows us to determine the rotation angle  $\theta$  for 3D points on any FOV to determine the deformation. In the first FOV the complete transformation is computed by an expression  $T = OL$ . And so on, for all other FOVs, transformation  $T^*$  is calculated analogously. The elementary matrix for the

transformed FOV is formulated below:

$$F = T^* F^0 T^{-1} \quad (10)$$

Here,  $F^0$  denotes the elementary matrix prior to carry out the transformations  $T$  and  $T^*$ .

#### D. Estimation and Incorporation of Liver Deformation

After computing linear transformation, we have used the following findings to estimate an affine deformation in our 3D template as:

$$y(Y, t) = M(t).Y + O(t) \quad (11)$$

where  $y$  is the position of a point in the 3D template,  $Y$  is the position in a reference pre-operative image,  $t$  is a time variable,  $T$  is the linear transformer computed in above subsection, and  $W$  is the translation.

To achieve smoothness in our resultant image, we have applied shading cues [48] on the deformed shape aforementioned formulations. Let us assume our liver surface is a Lambertian diffuse surface. To compute albedo  $\beta(u, v)$  of such surface, intensity of FOV defined by reflectance model is written as  $R(u, v)$  along the surface normal  $M(u, v)$  with the distant light source.

$$R : I(S(u, v)) = \beta(u, v) L \cot M(u, v) \quad (12)$$

Given FOV  $f$ ,  $f = 1, \dots, M$ , the albedo of deformed surface can be computed. So, the resultant rendered deformed 3D reconstructed liver surface is shown in Fig. 3.

#### E. Synthetic Deformation Model

We have evaluated the estimated liver deformation using a synthetic deformation model (SDM). It enables us to simulate surgeon's laparoscopic movement as in real MIS. Our SDM estimates  $Sh_e$ ,  $Ro_e$ ,  $Rp_e$  and  $Ed_e$  as shape, rotational, reprojection and edge errors for measuring deformation accuracy respectively. The shape and edge values in the 3D template vary with respect to different rotational and curvature values. The SDM is formally defined by a set of triplet vector as:

$$(Sh_e, Ro_e, Rp_e, Ed_e)_{e \in E}, E = 1, \dots, f \quad (13)$$

Given a set of vertex  $(Sh_e, Ro_e, Rp_e, Ed_e)$  the latest location of a vertex on 3D template mesh can be calculated as:

$$(\vec{u}_i \vec{u}_i^*) = w(Sh_e(Ro_e, Ed_e)u_i)u_i Rp_e, Ed_e + \in M_i \quad (14)$$

where  $u_i$  point has  $M_i$  as a unit normal at its surface,  $\in$  is the amount of movement for vertex over a tangent plane,  $w$  is the function which model the deformation over the  $u_i$ . In our setup, the geometrical locations of a 3D liver surface labeled manually act as ground truth (GT), and the reconstructed 3D liver surface is the calculated results with deformation.

The edge length error is calculated as difference of RMS summed norm of edge lengths between reconstructed 3D template and GT surface. The reprojection error is calculated as the norm of difference between the projected points in the 3D template and their correspondence in the resultant reconstructed image. A shape error  $Sh_e$  is defined as the root means RMS error on the corresponding point coordinates  $x, y, z$ , averaged over all the featured points and divided by the side length of the template mesh. The rotational error  $Ro_e$  is calculated as the angular distance between true and computed rotation as the smallest angle to make two rotations coincides. So the  $Ro_e$  is defined as the RMS angle distance averaged over all the FOVs and divided by the total rotational angle w.r.t. vertex  $(Sh_e, Ro_e, Rp_e, Ed_e)$ .

### III. RESULTS AND DISCUSSIONS

The implementation of this research was conducted on P3xlarge server instance provided by AWS (Amazon Web Service). It is set to a Tesla V100 GPU, 16 GB GPU memory, 10 virtual CPU. The operating system was 64-bit version of the 16.04LTS. The intra-operative FOVs with different angles were recorded using KARL STORZ laparoscope with a powerful 300 W Xenon light source. For 3D visualization of results, we have used 3D Slicer version 4.7.0 [49] which reconstruct deformed liver in 3D form with multiple viewpoints (sagittal, horizontal, and frontal plane) using iso-surface extraction. In 3D Slicer version 4.7.0, the frontal plane is perpendicular to the ground and separates the front (anterior) from the back (posterior). The horizontal plane is parallel to the ground and separates the head (superior) from the feet (inferior). The outcome of our model can be considered two-class prediction problem (binary classification), in which the outcomes are labeled either as positive ( $p$ ) and negative ( $n$ ). In this regard, there are four possible outcomes of our model. If the outcome from our model is  $p$  and the manually labeled ground truth is also  $p$ , then it is called a true positive ( $TP$ ) means correctly reconstructed; however, if the manually ground truth is  $n$  then it is said to be a false positive ( $FP$ ) means incorrectly reconstructed. On the contrary, a true negative ( $TN$ ) is a case when both our proposed model and manually labeled ground truth give  $n$  as an outcome indicating correctly rejected, and false negative ( $FN$ ) is the case of uncorrected rejection, which happens when our model gives  $n$  value while the output of manually labeled ground truth is  $p$ . The explanation of the above four possible outcomes ( $TP, TN, FP, FN$ ) according to our model is shown in Fig. 7.

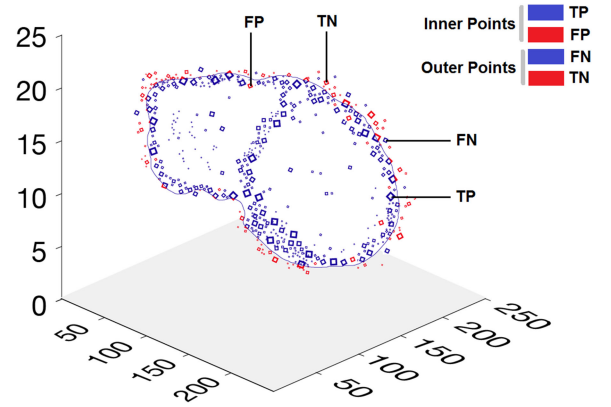


Fig. 7. Liver surface reconstruction result using our proposed method with incorporated estimated deformation. The blue squares inside the liver model are showing true positive (TP) for our model means correctly reconstructed; however blue squares outside the boundary of liver model are labeled as false positive (FP) means incorrectly reconstructed. On the contrary, a true negative (TN) is a case indicating red squares outside the liver boundary showing correct rejection, red squares inside the liver boundary are false negative (FN) in the case of uncorrected rejection.

#### A. Quantitative Evaluation

We have used precision and recall rates for drawing receiver operating characteristic (ROC) curve [50] to quantitatively analyze the performance of our method. Our evaluation setup draw ROC curve between the true positive rate (TPR) and the false positive rate (FPR) with different criteria for threshold. The true-positive rate is termed as sensitivity or recall [51] while the false-positive rate is known as the fall-out or precision. The formulation we used to calculate TPR and FPR is as follows:  $TPR = Recall = TP/TP + FN$  and  $FPR = Precision = FP/FP + TN$ . For our setup, precision is the percentage of correctly reconstructed liver area while recall measures the percentage of uncommon area among reconstructed and ground truth liver images.

*Effect of various degrees of motion on reconstruction:* Fig. 8(a) shows the ROC curve for analyzing various degrees of motion effect on the reconstructed resultant liver images. For this scenario the threshold  $T_m$  is set with respect to three degrees of motions  $m = \{0, 2.5, 5\}$ . In these cases, the same experiment is conducted to reconstruct liver image by finding corresponding points between deformed template and pre-operative liver images. By varying the degree of motion of the laparoscopic camera the number of detected corresponding points affects and as a result reconstructed liver image is affected. On each ROC curve one may see the performance of the following degrees of motion:

- $m_3 = 0$ , when the laparoscope is inserted for initialization of MIS process.
- $m_2 = 2.5$ , when the laparoscope is in preparation phase having slight motion.
- $m_1 = 5$ , when the laparoscope is in working phase having normal motion.

The ROC curves in Fig. 8(a) is showing the fair comparison between various degrees of laparoscopic camera motion. Each

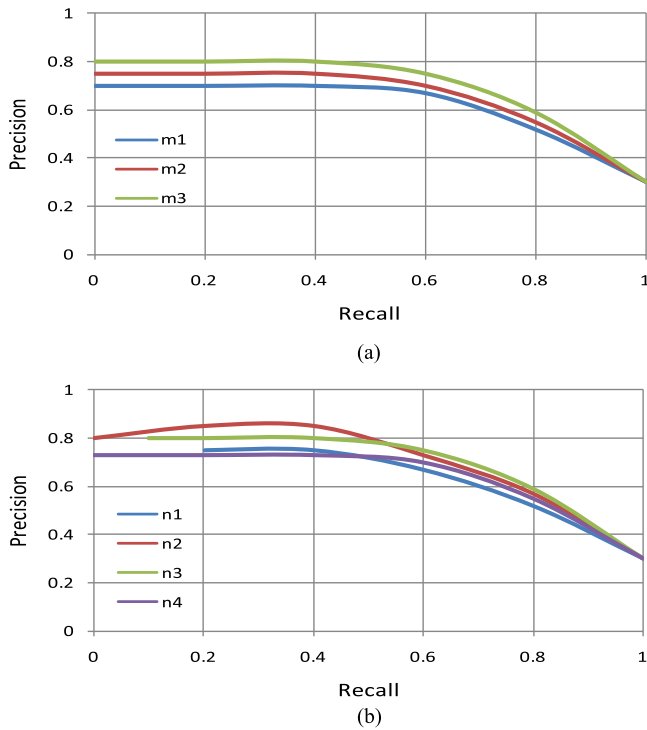


**Fig. 8.** Receiver operating characteristic (ROC) curve for estimating various affects of motion and noise on reconstruction results. (a) ROC for various degrees of motion  $m_1$ ,  $m_2$  and  $m_3$  showing precision plotted against recall with area under the curve (AUC) maximum for  $m_3$  at 0.7944. (b) ROC for different levels of noise  $n_1$ ,  $n_2$ ,  $n_3$  and  $n_4$  for estimating affects of noise on our proposed model.

point in ROC curve is obtained as the average TPR and FPR using a particular value of threshold  $T_m$  [50]. It is depicted from the figure that at  $m_3$  when there is almost no motion the liver surface do not undergo to deformation. For this scenario the comparison between template and pre-operative liver image found no matching points (corresponding points). While in case of  $m_2$ , when there is slight motion our method finds enough matching points to compare deformed template and pre-operative liver images. The ROC curve shows best performance when laparoscope is in working phase at  $m_1$ . The liver surface is fully deformed and our method found maximum matching points to calculate deformation across template and pre-operative images. To interpret the ROC curve, we have used area under the curve (AUC) to show best criteria.  $AUC = 0.5$  means the experiment is not informative, while  $AUC = 1$  means the experiment is perfect while its value from 0.7 to 0.9 means moderately accurate. Table II shows the values of AUC for  $m_3$ ,  $m_2$  and  $m_1$  are 0.71, 0.73 and 0.79 respectively. Hence, we have achieved best AUC for  $m_3$  i.e. 0.79 showing  $m_1$  is the best criteria for achieving accurate reconstruction results.

*Effect of various degrees of noise on reconstruction:* Fig. 8(b) shows the ROC plotted for interpreting the affects of various noise levels on reconstruction result. Threshold  $T_n$  for four criteria  $n = \{0, 10, 20, 30\}$  are selected. Noise in our proposed method, the presence of laparoscopic camera at surgical view which may pose difficulty to capture good quality FOV's during

**TABLE II**  
EFFECT OF VARIOUS DEGREES OF MOTION AND NOISE LEVELS ON RECONSTRUCTION. THREE CRITERIA  $m_1$ ,  $m_2$  AND  $m_3$  FOR SHOWING VARIABILITY OF MOTION INTENSITY AND FOUR CRITERIA  $n_1$ ,  $n_2$ ,  $n_3$  AND  $n_4$  FOR ESTIMATING NOISE AFFECTS WITH AVERAGED VALUES OF PRECISION, RECALL AND AUC ARE USED FOR STATISTICAL ANALYSIS

Motion Criteria	Precision	Recall	Auc
motion ( $m_1$ )	0.5983	0.5123	0.7134
motion ( $m_2$ )	0.6334	0.5013	0.7329
motion ( $m_3$ )	0.6431	0.5333	0.7944
noise ( $n_1$ )	0.6431	0.5333	0.7569
noise ( $n_2$ )	0.6233	0.5024	0.8311
noise ( $n_3$ )	0.6733	0.5233	0.8007
noise ( $n_4$ )	0.6839	0.5134	0.7229

Laparoscopy. In Fig. 8(b) the noise criteria are defined as  $n_1 = 0$  (no noise),  $n_2 = 10$  (low level light and small amount of blood due to little incision),  $n_3 = 20$  (in presence of full exposure of light),  $n_4 = 30$  (presence of blood and full exposure light). The AUC for the plot in Fig. 8(b) is showing that our method performs best when noise is low at  $n_2$ . Table II presents the AUC of all the four criteria. The presence of excessive noise is an implication of the proposed technique, in the future, we will enhance this work to calculate deformation accurately even in the presence of various noises.

## B. Qualitative Evaluation

To authenticate our method qualitatively, we have experimented on intra-operative FOVs of human liver. Our approach generated a 3D template of the liver during exploration phase of laparoscopy. Then, a set of complex and unpredictable deformations  $D_p$  occurred due to pneumoperitoneum and other surgical manipulations when the surgeon starts to examine the liver. See Fig. 7 for our results on liver surface reconstruction with deformation. First layer is showing intra-operative FOVs taken during liver surgery. Second layer is showing sparse points marked on liver area. Third layer is depicting dense points on liver area while fourth layer is indicating boundary formation using detected keypoints mesh. Last layer is showing comparison between pre-operative and reconstructed liver to incorporate deformation in the resultant reconstructed liver. We have determined the liver deformation using the corresponding point match difference (CPMD) in every vertex of 3D template mesh and pre-operative image. It is obvious from Fig. 9 that the displacement level differed significantly across each region of the liver. Fig. 9(b) and (c) depict that the anterior and posterior view displacements are relatively larger than the superior and inferior views of the liver.

We measured the error between reconstructed and the GT mesh by computing the distance between the two meshes corresponding vertices. Fig. 9(c) shows feature points and a deformed new mesh. As expected, in the case of dense feature correspondences, our proposed technique outperforms state-of-the-art. When the number of correspondences is increased as shown in Fig. 9(a) and (b), in the deformed regions, proposed method tends to be as accurate as the real-time results. Fig. 7

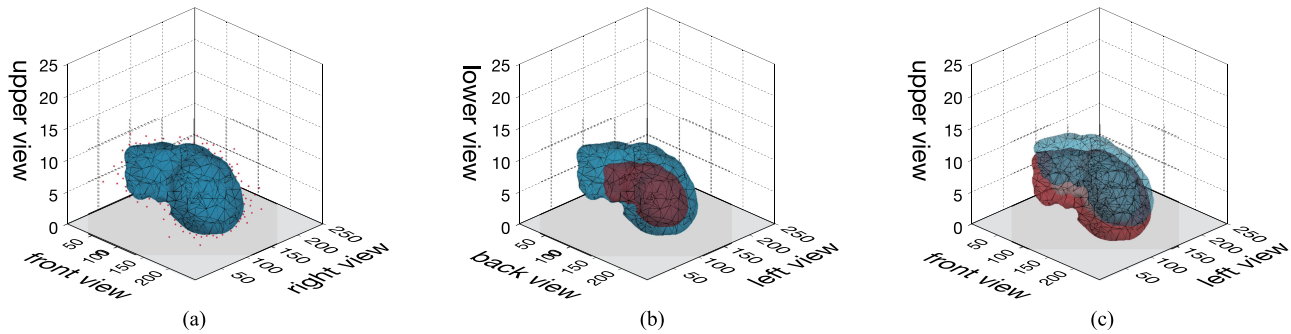


**Fig. 9.** Qualitative results of our proposed approach with respect to variable view-points of liver. Upper: superior, lower: inferior, front: anterior, back: posterior, right and left. (a) 3D template mesh with red boundary line and outside liver unmatched keypoints are colored blue. (b) The inner liver is a 3D model extracted from pre-operative CT data using Slicer; outer blue liver is the 3D template for finding correspondence points (edges of dark black lines). (c) Deformed image comparable to pre-operative extracted liver model, the upper blue boundary and inner light red patch is showing the estimated deformation.

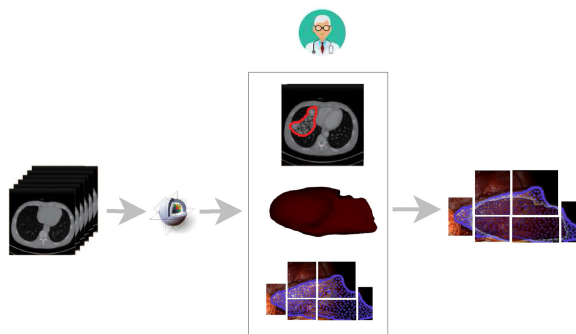


**Fig. 10.** Manual validation of reconstruction results for the proposed model. We have extracted liver model from pre-operative CTA volumes using Slicer. Ground truth (GT) is in the form of manually labeled liver images. The medical expert from cooperative hospital validates the pre-operative, GT and resultant reconstructed liver images and give his opinion on validation results before use in intra-operative environment.

qualitatively shows our fine improvement on the recovery of deformed 3D liver reconstruction.

### C. Comparison With State-of-the-Art

We have compared precision and accuracy of our method using four metrics named Positive Predictive Value (PPV), Negative predictive value (NPV), false omission rate (FOR) and Root Mean Square Error (RMSE) with five state-of-the-art approaches such as DSFM used by Pilet *et al.* [48] and Pizarro and Bartoli [41], DSFMS implemented by Malti *et al.* [37] and Laura *et al.* [38], and SFS by Turan *et al.* [52]. RMSE measures accuracy by calculating the differences between resultant reconstructed image and the values observed in corresponding manually labeled ground truth liver image as shown in Fig. 10. In our case the differences are in terms of four errors i.e. edge length ( $E_d$ ), reprojection ( $R_p$ ), shape ( $S_h$ ) and rotational ( $R_o$ ) using SDM model. Table III summarizes the errors values measured for our setup. We have taken the summed norm of all the above-mentioned errors to calculate value of RMSE shown in Table III. RMSE is chosen as error metrics because it serves to give cumulative magnitudes of the errors into a single measure.

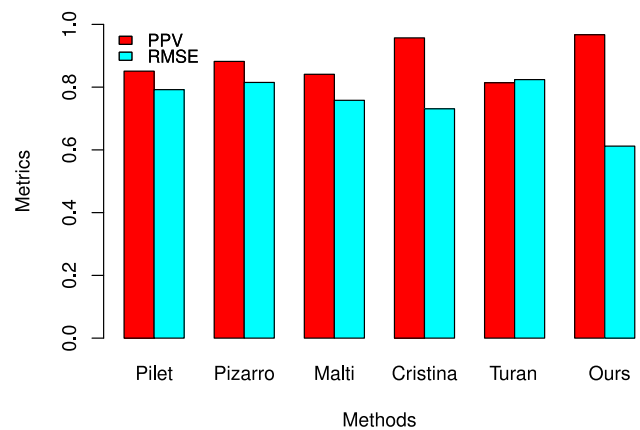


**Fig. 11.** Comparison of the proposed model with five state-of-the-art techniques in terms of PPV and RMSE. It is obvious from the bar metrics that our method achieves high performance in terms of increased PPV and lowest RMSE error as compared to other five methods.

Figs. 11 and 12 depict that our method shows minimal errors as compare to other techniques. Although DSFMS's performance is outstanding, yet our technique has achieved remarkable results in terms of shape and rotational errors. The precision of this research has been estimated using the positive predictive value (PPV) [38], formulated as  $PPV = TP/TP + FP$ , negative predictive value (NPV) formulated as  $TN/TN + FN$  and false omission rate (FOR) formulated as  $(1 - NPV)$ . As it is shown in Fig. 7, the true positives (TP) represent the intersection between deformed liver template and pre-operative liver. The false positives (FP) on the contrary are those areas in Fig. 7 which are not common in pre-operative liver and deformed template. The results of RMSE, NPV, FOR and PPV measured for 50 CTA volumes are shown in Table III. It is obvious from Table III that we have achieved highest precision in terms of maximum PPV value of 0.92 and NPV value of 0.90 and improved accuracy with lowest RMSE values than the state-of-the-art. It takes almost 20–30 seconds to perform a single 3D reconstruction for liver on Tesla V100 GPU which proves to be a prospective clinical importance of the proposed method.

TABLE III

COMPARISON OF OUR MODEL TO EVALUATE PRECISION AND ACCURACY WITH STATE-OF-THE-ART. WE HAVE USED POSITIVE PREDICTIVE VALUE (PPV), NEGATIVE PREDICTIVE VALUE (NPV) AND FALSE OMISSION RATE (FOR) FOR ESTIMATING PRECISION AND ROOT MEAN SQUARE ERROR (RMSE) FOR EDGE-LENGTH ( $Ed_e$ ), ROTATIONAL ( $Ro_e$ ), SHAPE ( $Sh_e$ ) AND REPROJECTION ( $Rp_e$ ) ARE CALCULATED FOR MEASURING ACCURACY

Method	PPV	NPV	FOR	RMS ( $Ed_e$ )	RMS ( $Ro_e$ )	RMS ( $Sh_e$ )	RMS ( $Rp_e$ )
Pilet et al. [44]	0.89±0.62	0.85±0.74	0.15±0.79	0.61±0.32	0.58±0.78	0.62±0.13	0.42±0.23
Pizarro and Bartoli [37]	0.79±0.92	0.88±0.73	0.12±0.74	0.41±0.95	0.43±0.68	0.56±0.14	0.49±0.13
Malti et al. [33]	0.82±0.15	0.86±1.02	0.14±0.98	0.42±0.69	0.61±0.43	0.32±0.11	0.45±0.73
Laura et al. [34]	0.87±0.43	0.82±0.49	0.18±0.43	0.40±0.53	0.51±0.12	0.44±0.13	0.33±0.24
Turan et al. [48]	0.85±0.45	0.81±0.33	0.19±0.33	0.58±0.23	0.56±0.33	0.80±0.53	0.64±0.13
Our Method	0.92±0.34	0.90±0.23	0.10±0.24	0.23±0.11	0.35±0.13	0.18±0.10	0.22±0.09

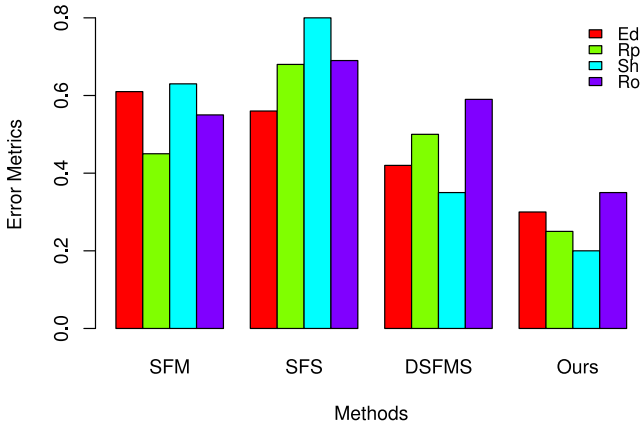


Fig. 12. Comparison of the proposed technique with three state-of-the-art methods in terms of edge-length ( $Ed_e$ ), rotational ( $Ro_e$ ), shape ( $Sh_e$ ) and reprojection ( $Rp_e$ ) errors. The values in the graph shows that our method outperforms all the three previous techniques by lowering the errors to achieve improved accuracy for reconstruction.

#### IV. CONCLUSION

3D reconstruction during MIS poses several specific challenges such as liver tissue deformation and retraction of other internal organs due to surgical interventions. These limitations make feature detection and matching techniques insufficient solution to determine the intra-operative morphology and motion of liver tissues. In this article, we report a comprehensive approach for solving liver deformation issue. Our method uses the SFM with shading cues to finely tune the 3D reconstruction. Essential mathematical formulation for estimating deformation specified to each step of proposed technique has been discussed. The accuracy of the proposed technique is verified quantitatively using SDM and qualitatively on real in-vivo liver images. The advantage of using our technique compared to other active techniques is that it does not require modification of standard laparoscopes hardware. Our approach is an answer to the need for better visualization and reliable shape recovery during laparoscopic surgery. The obtained reconstruction error is low enough to encourage further research. An interesting avenue for future research is applying a template-free approach to retrieve 3D reconstruction in real time during laparoscopy.

#### REFERENCES

[1] K. Fujii et al., "Gaze gesture based human robot interaction for laparoscopic surgery," *Med Image Anal.*, vol. 44, pp. 196–214, 2018.

[2] J. H. Chandler et al., "Real-time assessment of mechanical tissue trauma in surgery," *IEEE Trans. Biomed. Eng.*, vol. 64, no. 10, pp. 2384–2393, Oct. 2017.

[3] A. Karambakhsh et al., "Deep gesture interaction for augmented anatomy learning," *Int. J. Inf. Manage.*, vol. 45, pp. 328–336, Apr. 2019.

[4] A. Kamel et al., "Deep convolutional neural networks for human action recognition using depth maps and postures," *IEEE Trans. Syst., Man, Cybern., Syst.*, to be published, doi: 10.1109/TSMC.2018.2850149.

[5] Y. Wen et al., "Deep color guided coarse-to-fine convolutional network cascade for depth image super-resolution," *IEEE Trans. Image Process.*, vol. 28, no. 2, pp. 994–1006, Feb. 2019.

[6] P. Ghaderi and H. R. Marateb, "Muscle activity map reconstruction from high density surface EMG signals with missing channels using image inpainting and surface reconstruction methods," *IEEE Trans. Biomed. Eng.*, vol. 64, no. 7, pp. 1513–1523, Jul. 2017.

[7] J. Fan et al., "EEG-based affect and workload recognition in a virtual driving environment for ASD intervention," *IEEE Trans. Biomed. Eng.*, vol. 65, no. 1, pp. 43–51, Jan. 2018.

[8] P. J. Edwards et al., "Design and evaluation of a system for microscope-assisted guided interventions (MAGI)," in *Proc. Int. Conf. Med. Image Comput. Comput. Assisted Intervention*, 1999, pp. 842–851.

[9] M. Bajura et al., "Merging virtual objects with the real world: Seeing ultrasound imagery within the patient," *ACM SIGGRAPH Comput. Graph.*, vol. 26, no. 2, pp. 203–210, 1992.

[10] S. Thompson et al., "Accuracy validation of an image guided laparoscopy system for liver resection," *Proc. SPIE*, 2015, vol. 9415, Art. no. 941509.

[11] P. Pratt et al., "An effective visualisation and registration system for image-guided robotic partial nephrectomy," *J. Robot. Surgery*, vol. 6, no. 1, pp. 23–31, 2012.

[12] A. Kamel et al., "An investigation of 3D human pose estimation for learning Tai Chi: A human factor perspective," *Int. J. Human-Comput. Interact.*, vol. 35, no. 4–5, pp. 427–439, 2019.

[13] N. Tsutsumi et al., "Image-guided laparoscopic surgery in an open MRI operating theater," *Surg. Endoscopy*, vol. 27, no. 6, pp. 2178–2184, 2013.

[14] O. van Kaick et al., "A survey on shape correspondence," *Comput. Graph. Forum*, vol. 30, no. 6, pp. 1681–1707, 2011.

[15] S. Röhl et al., "Dense GPU-enhanced surface reconstruction from stereo endoscopic images for intraoperative registration," *Med Phys.*, vol. 39, no. 3, pp. 1632–1645, 2012.

[16] T. Heimann et al., "Comparison and evaluation of methods for liver segmentation from CT datasets," *IEEE Trans. Med. Imag.*, vol. 28, no. 8, pp. 1251–1265, Aug. 2009.

[17] A. B. Benincasa et al., "Feasibility study for image-guided kidney surgery: Assessment of required intraoperative surface for accurate physical to image space registrations," *Med. Phys.*, vol. 35, no. 9, pp. 4251–4261, 2008.

[18] G. A. Puerto-Souza and G. L. Mariottini, "A fast and accurate feature-matching algorithm for minimally-invasive endoscopic images," *IEEE Trans. Med. Imag.*, vol. 32, no. 7, pp. 1201–1214, Jul. 2013.

[19] A. L. Simpson et al., "Model-assisted image-guided liver surgery using sparse intraoperative data," in *Soft Tissue Biomechanical Modeling for Computer Assisted Surgery*. Berlin, Germany: Springer, 2012, pp. 7–40.

[20] N. Haouchine et al., "Image-guided simulation of heterogeneous tissue deformation for augmented reality during hepatic surgery," in *Proc. IEEE Int. Symp. Mixed Augmented Reality*, 2013, pp. 199–208.

[21] R. Plantefève et al., "Automatic alignment of pre and intraoperative data using anatomical landmarks for augmented laparoscopic liver surgery," in *Proc. Int. Symp. Biomed. Simul.*, 2014, pp. 58–66.

[22] B. Vagvolgyi et al., "Video to CT registration for image overlay on solid organs," in *Augmented Reality in Medical Imaging and Augmented Reality in Computer-Aided Surgery*. Berlin, Germany: Springer, 2008, pp. 78–86.

- [23] S. Suwelack *et al.*, "Physics-based shape matching for intraoperative image guidance," *Med. Phys.*, vol. 41, no. 11, 2014, Art. no. 111901.
- [24] N. Haouchine *et al.*, "Using contours as boundary conditions for elastic registration during minimally invasive hepatic surgery," in *Proc. IEEE/RSJ Int. Conf. Intell. Robots Syst.*, 2016, pp. 495–500.
- [25] D. Wang and A. H. Tewfik, "Real time 3D visualization of intraoperative organ deformations using structured dictionary," *IEEE Trans. Med. Imag.*, vol. 31, no. 4, pp. 924–937, Apr. 2012.
- [26] S. Bernhardt *et al.*, "The status of augmented reality in laparoscopic surgery as of 2016," *Med. Image Anal.*, vol. 37, pp. 66–90, 2017.
- [27] J. Marescaux, F. Rubino, M. Arenas, D. Mutter, and L. Soler, "Augmented-reality-assisted laparoscopic adrenalectomy," *JAMA*, vol. 292, no. 18, pp. 2211–2215, 2004.
- [28] K. Konishi *et al.*, "A real-time navigation system for laparoscopic surgery based on three-dimensional ultrasound using magneto-optic hybrid tracking configuration," *Int. J. Comput. Assisted Radiol. Surgery*, vol. 2, no. 1, pp. 1–10, 2007.
- [29] R. Mårvik *et al.*, "Laparoscopic navigation pointer for three-dimensional image-guided surgery," *Surg. Endoscopy*, vol. 18, no. 8, pp. 1242–1248, 2004.
- [30] M. Schwenke *et al.*, "Fast numerical simulation of focused ultrasound treatments during respiratory motion with discontinuous motion boundaries," *IEEE Trans. Biomed. Eng.*, vol. 64, no. 7, pp. 1455–1468, Jul. 2017.
- [31] K. Weigand *et al.*, "In vivo electrophysiological study of induced ventricular tachycardia in intact rat model of chronic ischemic heart failure," *IEEE Trans. Biomed. Eng.*, vol. 64, no. 6, pp. 1393–1399, Jun. 2017.
- [32] M. Hajiaghayi *et al.*, "A 3-D active contour method for automated segmentation of the left ventricle from magnetic resonance images," *IEEE Trans. Biomed. Eng.*, vol. 64, no. 1, pp. 134–144, Jan. 2017.
- [33] S. Apostolopoulos and R. Sznitman, "Efficient OCT volume reconstruction from slitlamp microscopes," *IEEE Trans. Biomed. Eng.*, vol. 64, no. 10, pp. 2403–2410, Oct. 2017.
- [34] W. Cong *et al.*, "Quantitative analysis of deformable model-based 3-D reconstruction of coronary artery from multiple angiograms," *IEEE Trans. Biomed. Eng.*, vol. 62, no. 8, pp. 2079–2090, Aug. 2015.
- [35] L. Maier-Hein *et al.*, "Optical techniques for 3D surface reconstruction in computer-assisted laparoscopic surgery," *Med. Image Anal.*, vol. 17, no. 8, pp. 974–996, 2013.
- [36] L. Yu *et al.*, "Three-dimensional noninvasive imaging of ventricular arrhythmias in patients with premature ventricular contractions," *IEEE Trans. Biomed. Eng.*, vol. 65, no. 7, pp. 1495–1503, Jul. 2018.
- [37] A. Malti *et al.*, "Template-based conformal shape-from-motion-and-shading for laparoscopy," in *Proc. Int. Conf. Inf. Process. Comput.-Assisted Interventions*, 2012, pp. 1–10.
- [38] C. O. Laura *et al.*, "Accurate physics-based registration for the outcome validation of minimal invasive interventions and open liver surgeries," *IEEE Trans. Biomed. Eng.*, vol. 64, no. 2, pp. 362–371, Feb. 2017.
- [39] P. K. Saha *et al.*, "Iso-shaping rigid bodies for estimating their motion from image sequences," *IEEE Trans. Med. Imag.*, vol. 23, no. 1, pp. 63–72, Jan. 2004.
- [40] M. Hu *et al.*, "Reconstruction of a 3D surface from video that is robust to missing data and outliers: Application to minimally invasive surgery using stereo and mono endoscopes," *Med Image Anal.*, vol. 16, no. 3, pp. 597–611, 2012.
- [41] D. Pizarro and A. Bartoli, "Feature-based deformable surface detection with self-occlusion reasoning," *Int. J. Comput. Vis.*, vol. 97, no. 1, pp. 54–70, 2012.
- [42] J. M. Marcinczak *et al.*, "A robust motion estimation system for minimal invasive laparoscopy," *Proc. SPIE*, 2012, vol. 8316, Art. no. 83162L.
- [43] D. G. Lowe, "Distinctive image features from scale-invariant keypoints," *Int. J. Comput. Vis.*, vol. 60, no. 2, pp. 91–110, 2004.
- [44] A. Shahrokhni *et al.*, "Bundle adjustment for markerless body tracking in monocular video sequences," in *Proc. ISPRS Workshop Vis. Animation Reality-Based 3D Models*, 2003, pp. 1–6.
- [45] M. Muja and D. G. Lowe, "Scalable nearest neighbor algorithms for high dimensional data," *IEEE Trans. Pattern Anal. Mach. Intell.*, vol. 36, no. 11, pp. 2227–2240, Nov. 2014.
- [46] M. J. Westoby *et al.*, "'Structure-from-motion' photogrammetry: A low-cost, effective tool for geoscience applications," *Geomorphology*, vol. 179, pp. 300–314, 2012.
- [47] A. Johansson *et al.*, "Rigidbody motion correction of the liver in image reconstruction for golden-angle stack-of-stars DCE MRI," *Mag. Reson. Med.*, vol. 79, no. 3, pp. 1345–1353, 2018.
- [48] J. Pilet *et al.*, "Fast non-rigid surface detection, registration and realistic augmentation," *Int. J. Comput. Vis.*, vol. 76, no. 2, pp. 109–122, 2008.
- [49] X. Chen *et al.*, "3D printing and modelling of customized implants and surgical guides for non-human primates," *J. Neurosci. Methods*, vol. 286, pp. 38–55, 2017.
- [50] M.-M. Cheng *et al.*, "Global contrast based salient region detection," *IEEE Trans. Pattern Anal. Mach. Intell.*, vol. 37, no. 3, pp. 569–582, Mar. 2015.
- [51] W. Qi *et al.*, "SaliencyRank: Two-stage manifold ranking for salient object detection," *Comput. Vis. Media*, vol. 1, no. 4, pp. 309–320, 2015.
- [52] M. Turan *et al.*, "A fully dense and globally consistent 3D map reconstruction approach for GI tract to enhance therapeutic relevance of the endoscopic capsule robot," unpublished paper, 2017, arXiv:1705.06524.